

Dalitz-plot Analysis of $B^0 \rightarrow \bar{D}^0 \pi^+ \pi^-$

P. del Amo Sanchez,¹ J. P. Lees,¹ V. Poireau,¹ E. Prencipe,¹ V. Tisserand,¹ J. Garra Tico,² E. Grauges,² M. Martinelli^{ab,3} A. Palano^{ab,3} M. Pappagallo^{ab,3} G. Eigen,⁴ B. Stugu,⁴ L. Sun,⁴ M. Battaglia,⁵ D. N. Brown,⁵ B. Hooberman,⁵ L. T. Kerth,⁵ Yu. G. Kolomensky,⁵ G. Lynch,⁵ I. L. Osipenkov,⁵ T. Tanabe,⁵ C. M. Hawkes,⁶ A. T. Watson,⁶ H. Koch,⁷ T. Schroeder,⁷ D. J. Asgeirsson,⁸ C. Hearty,⁸ T. S. Mattison,⁸ J. A. McKenna,⁸ A. Khan,⁹ A. Randle-Conde,⁹ V. E. Blinov,¹⁰ A. R. Buzykaev,¹⁰ V. P. Druzhinin,¹⁰ V. B. Golubev,¹⁰ A. P. Onuchin,¹⁰ S. I. Serednyakov,¹⁰ Yu. I. Skovpen,¹⁰ E. P. Solodov,¹⁰ K. Yu. Todyshev,¹⁰ A. N. Yushkov,¹⁰ M. Bondioli,¹¹ S. Curry,¹¹ D. Kirkby,¹¹ A. J. Lankford,¹¹ M. Mandelkern,¹¹ E. C. Martin,¹¹ D. P. Stoker,¹¹ H. Atmacan,¹² J. W. Gary,¹² F. Liu,¹² O. Long,¹² G. M. Vitug,¹² C. Campagnari,¹³ T. M. Hong,¹³ D. Kovalskiy,¹³ J. D. Richman,¹³ A. M. Eisner,¹⁴ C. A. Heusch,¹⁴ J. Kroseberg,¹⁴ W. S. Lockman,¹⁴ A. J. Martinez,¹⁴ T. Schalk,¹⁴ B. A. Schumm,¹⁴ A. Seiden,¹⁴ L. O. Winstrom,¹⁴ C. H. Cheng,¹⁵ D. A. Doll,¹⁵ B. Echenard,¹⁵ D. G. Hitlin,¹⁵ P. Ongmongkolkul,¹⁵ F. C. Porter,¹⁵ A. Y. Rakitin,¹⁵ R. Andreassen,¹⁶ M. S. Dubrovin,¹⁶ G. Mancinelli,¹⁶ B. T. Meadows,¹⁶ M. D. Sokoloff,¹⁶ P. C. Bloom,¹⁷ W. T. Ford,¹⁷ A. Gaz,¹⁷ M. Nagel,¹⁷ U. Nauenberg,¹⁷ J. G. Smith,¹⁷ S. R. Wagner,¹⁷ R. Ayad,^{18,*} W. H. Toki,¹⁸ T. M. Karbach,¹⁹ J. Merkel,¹⁹ A. Petzold,¹⁹ B. Spaan,¹⁹ K. Wacker,¹⁹ M. J. Kobel,²⁰ K. R. Schubert,²⁰ R. Schwierz,²⁰ D. Bernard,²¹ M. Verderi,²¹ P. J. Clark,²² S. Playfer,²² J. E. Watson,²² M. Andreotti^{ab,23} D. Bettoni^{a,23} C. Bozzi^{a,23} R. Calabrese^{ab,23} A. Cecchi^{ab,23} G. Cibinetto^{ab,23} E. Fioravanti^{ab,23} P. Franchini^{ab,23} E. Luppi^{ab,23} M. Munerato^{ab,23} M. Negrini^{ab,23} A. Petrella^{ab,23} L. Piemontese^{a,23} R. Baldini-Ferrolì,²⁴ A. Calcaterra,²⁴ R. de Sangro,²⁴ G. Finocchiaro,²⁴ M. Nicolaci,²⁴ S. Pacetti,²⁴ P. Patteri,²⁴ I. M. Peruzzi,^{24,†} M. Piccolo,²⁴ M. Rama,²⁴ A. Zallo,²⁴ R. Contri^{ab,25} E. Guido^{ab,25} M. Lo Vetere^{ab,25} M. R. Monge^{ab,25} S. Passaggio^{a,25} C. Patrignani^{ab,25} E. Robutti^{a,25} S. Tosi^{ab,25} B. Bhuyan,²⁶ V. Prasad,²⁶ C. L. Lee,²⁷ M. Morii,²⁷ A. Adametz,²⁸ J. Marks,²⁸ U. Uwer,²⁸ F. U. Bernlochner,²⁹ M. Ebert,²⁹ H. M. Lacker,²⁹ T. Lueck,²⁹ A. Volk,²⁹ P. D. Dauncey,³⁰ M. Tibbetts,³⁰ P. K. Behera,³¹ U. Mallik,³¹ C. Chen,³² J. Cochran,³² H. B. Crawley,³² L. Dong,³² W. T. Meyer,³² S. Prell,³² E. I. Rosenberg,³² A. E. Rubin,³² A. V. Gritsan,³³ Z. J. Guo,³³ N. Arnaud,³⁴ M. Davier,³⁴ D. Derkach,³⁴ J. Firmino da Costa,³⁴ G. Grosdidier,³⁴ F. Le Diberder,³⁴ A. M. Lutz,³⁴ B. Malaescu,³⁴ A. Perez,³⁴ P. Roudeau,³⁴ M. H. Schune,³⁴ J. Serrano,³⁴ V. Sordini,^{34,‡} A. Stocchi,³⁴ L. Wang,³⁴ G. Wormser,³⁴ D. J. Lange,³⁵ D. M. Wright,³⁵ I. Bingham,³⁶ C. A. Chavez,³⁶ J. P. Coleman,³⁶ J. R. Fry,³⁶ E. Gabathuler,³⁶ R. Gamet,³⁶ D. E. Hutchcroft,³⁶ D. J. Payne,³⁶ C. Touramanis,³⁶ A. J. Bevan,³⁷ F. Di Lodovico,³⁷ R. Sacco,³⁷ M. Sigamani,³⁷ G. Cowan,³⁸ S. Paramesvaran,³⁸ A. C. Wren,³⁸ D. N. Brown,³⁹ C. L. Davis,³⁹ A. G. Denig,⁴⁰ M. Fritsch,⁴⁰ W. Gradl,⁴⁰ A. Hafner,⁴⁰ K. E. Alwyn,⁴¹ D. Bailey,⁴¹ R. J. Barlow,⁴¹ G. Jackson,⁴¹ G. D. Lafferty,⁴¹ T. J. West,⁴¹ J. Anderson,⁴² R. Cenci,⁴² A. Jawahery,⁴² D. A. Roberts,⁴² G. Simi,⁴² J. M. Tuggle,⁴² C. Dallapiccola,⁴³ E. Salvati,⁴³ R. Cowan,⁴⁴ D. Dujmic,⁴⁴ G. Sciolla,⁴⁴ M. Zhao,⁴⁴ D. Lindemann,⁴⁵ P. M. Patel,⁴⁵ S. H. Robertson,⁴⁵ M. Schram,⁴⁵ P. Biassoni^{ab,46} A. Lazzaro^{ab,46} V. Lombardo^{a,46} F. Palombo^{ab,46} S. Stracka^{ab,46} L. Cremaldi,⁴⁷ R. Godang,^{47,§} R. Kroeger,⁴⁷ P. Sonnek,⁴⁷ D. J. Summers,⁴⁷ X. Nguyen,⁴⁸ M. Simard,⁴⁸ P. Taras,⁴⁸ G. De Nardo^{ab,49} D. Monorchio^{ab,49} G. Onorato^{ab,49} C. Sciacca^{ab,49} G. Raven,⁵⁰ H. L. Snoek,⁵⁰ C. P. Jessop,⁵¹ K. J. Knoepfel,⁵¹ J. M. LoSecco,⁵¹ W. F. Wang,⁵¹ L. A. Corwin,⁵² K. Honscheid,⁵² R. Kass,⁵² J. P. Morris,⁵² N. L. Blount,⁵³ J. Brau,⁵³ R. Frey,⁵³ O. Igonkina,⁵³ J. A. Kolb,⁵³ R. Rahmat,⁵³ N. B. Sinev,⁵³ D. Strom,⁵³ J. Strube,⁵³ E. Torrence,⁵³ G. Castelli^{ab,54} E. Feltresi^{ab,54} N. Gagliardi^{ab,54} M. Margoni^{ab,54} M. Morandin^{a,54} M. Posocco^{a,54} M. Rotondo^{a,54} F. Simonetto^{ab,54} R. Stroili^{ab,54} E. Ben-Haim,⁵⁵ G. R. Bonneaud,⁵⁵ H. Briand,⁵⁵ G. Calderini,⁵⁵ J. Chauveau,⁵⁵ O. Hamon,⁵⁵ Ph. Leruste,⁵⁵ G. Marchiori,⁵⁵ J. Ocariz,⁵⁵ J. Prendki,⁵⁵ S. Sitt,⁵⁵ M. Biasini^{ab,56} E. Manoni^{ab,56} A. Rossi^{ab,56} C. Angelini^{ab,57} G. Batignani^{ab,57} S. Bettarini^{ab,57} M. Carpinelli^{ab,57,¶} G. Casarosa^{ab,57} A. Cervelli^{ab,57} F. Forti^{ab,57} M. A. Giorgi^{ab,57} A. Lusiani^{ac,57} N. Neri^{ab,57} E. Paoloni^{ab,57} G. Rizzo^{ab,57} J. J. Walsh^{a,57} D. Lopes Pegna,⁵⁸ C. Lu,⁵⁸ J. Olsen,⁵⁸ A. J. S. Smith,⁵⁸ A. V. Telnov,⁵⁸ F. Anulli^{a,59} E. Baracchini^{ab,59} G. Cavoto^{a,59} R. Faccini^{ab,59} F. Ferrarotto^{a,59} F. Ferroni^{ab,59} M. Gaspero^{ab,59} L. Li Gioi^{a,59} M. A. Mazzoni^{a,59} G. Piredda^{a,59} F. Renga^{ab,59} T. Hartmann,⁶⁰ T. Leddig,⁶⁰ H. Schröder,⁶⁰ R. Waldi,⁶⁰ T. Adye,⁶¹ B. Franek,⁶¹ E. O. Olaiya,⁶¹ F. F. Wilson,⁶¹ S. Emery,⁶² G. Hamel de Monchenault,⁶² G. Vasseur,⁶² Ch. Yèche,⁶² M. Zito,⁶² M. T. Allen,⁶³ D. Aston,⁶³ D. J. Bard,⁶³ R. Bartoldus,⁶³ J. F. Benitez,⁶³ C. Cartaro,⁶³ M. R. Convery,⁶³ J. Dorfan,⁶³ G. P. Dubois-Felsmann,⁶³ W. Dunwoodie,⁶³ R. C. Field,⁶³ M. Franco Sevilla,⁶³ B. G. Fulsom,⁶³

A. M. Gabareen,⁶³ M. T. Graham,⁶³ P. Grenier,⁶³ C. Hast,⁶³ W. R. Innes,⁶³ M. H. Kelsey,⁶³ H. Kim,⁶³ P. Kim,⁶³ M. L. Kocian,⁶³ D. W. G. S. Leith,⁶³ S. Li,⁶³ B. Lindquist,⁶³ S. Luitz,⁶³ V. Luth,⁶³ H. L. Lynch,⁶³ D. B. MacFarlane,⁶³ H. Marsiske,⁶³ D. R. Muller,⁶³ H. Neal,⁶³ S. Nelson,⁶³ C. P. O'Grady,⁶³ I. Ofte,⁶³ M. Perl,⁶³ T. Pulliam,⁶³ B. N. Ratcliff,⁶³ A. Roodman,⁶³ A. A. Salnikov,⁶³ V. Santoro,⁶³ R. H. Schindler,⁶³ J. Schwiening,⁶³ A. Snyder,⁶³ D. Su,⁶³ M. K. Sullivan,⁶³ S. Sun,⁶³ K. Suzuki,⁶³ J. M. Thompson,⁶³ J. Va'vra,⁶³ A. P. Wagner,⁶³ M. Weaver,⁶³ C. A. West,⁶³ W. J. Wisniewski,⁶³ M. Wittgen,⁶³ D. H. Wright,⁶³ H. W. Wulsin,⁶³ A. K. Yarritu,⁶³ C. C. Young,⁶³ V. Ziegler,⁶³ X. R. Chen,⁶⁴ W. Park,⁶⁴ M. V. Purohit,⁶⁴ R. M. White,⁶⁴ J. R. Wilson,⁶⁴ S. J. Sekula,⁶⁵ M. Bellis,⁶⁶ P. R. Burchat,⁶⁶ A. J. Edwards,⁶⁶ T. S. Miyashita,⁶⁶ S. Ahmed,⁶⁷ M. S. Alam,⁶⁷ J. A. Ernst,⁶⁷ B. Pan,⁶⁷ M. A. Saeed,⁶⁷ S. B. Zain,⁶⁷ N. Guttman,⁶⁸ A. Soffer,⁶⁸ P. Lund,⁶⁹ S. M. Spanier,⁶⁹ R. Eckmann,⁷⁰ J. L. Ritchie,⁷⁰ A. M. Ruland,⁷⁰ C. J. Schilling,⁷⁰ R. F. Schwitters,⁷⁰ B. C. Wray,⁷⁰ J. M. Izen,⁷¹ X. C. Lou,⁷¹ F. Bianchi^{ab,72} D. Gamba^{ab,72} M. Pelliccioni^{ab,72} M. Bomben^{ab,73} L. Lanceri^{ab,73} L. Vitale^{ab,73} N. Lopez-March,⁷⁴ F. Martinez-Vidal,⁷⁴ D. A. Milanes,⁷⁴ A. Oyanguren,⁷⁴ J. Albert,⁷⁵ Sw. Banerjee,⁷⁵ H. H. F. Choi,⁷⁵ K. Hamano,⁷⁵ G. J. King,⁷⁵ R. Kowalewski,⁷⁵ M. J. Lewczuk,⁷⁵ I. M. Nugent,⁷⁵ J. M. Roney,⁷⁵ R. J. Sobie,⁷⁵ T. J. Gershon,⁷⁶ P. F. Harrison,⁷⁶ T. E. Latham,⁷⁶ E. M. T. Puccio,⁷⁶ H. R. Band,⁷⁷ S. Dasu,⁷⁷ K. T. Flood,⁷⁷ Y. Pan,⁷⁷ R. Prepost,⁷⁷ C. O. Vuosalo,⁷⁷ and S. L. Wu⁷⁷

(The BABAR Collaboration)

¹Laboratoire d'Annecy-le-Vieux de Physique des Particules (LAPP),

Université de Savoie, CNRS/IN2P3, F-74941 Annecy-Le-Vieux, France

²Universitat de Barcelona, Facultat de Física, Departament ECM, E-08028 Barcelona, Spain

³INFN Sezione di Bari^a; Dipartimento di Fisica, Università di Bari^b, I-70126 Bari, Italy

⁴University of Bergen, Institute of Physics, N-5007 Bergen, Norway

⁵Lawrence Berkeley National Laboratory and University of California, Berkeley, California 94720, USA

⁶University of Birmingham, Birmingham, B15 2TT, United Kingdom

⁷Ruhr Universität Bochum, Institut für Experimentalphysik 1, D-44780 Bochum, Germany

⁸University of British Columbia, Vancouver, British Columbia, Canada V6T 1Z1

⁹Brunel University, Uxbridge, Middlesex UB8 3PH, United Kingdom

¹⁰Budker Institute of Nuclear Physics, Novosibirsk 630090, Russia

¹¹University of California at Irvine, Irvine, California 92697, USA

¹²University of California at Riverside, Riverside, California 92521, USA

¹³University of California at Santa Barbara, Santa Barbara, California 93106, USA

¹⁴University of California at Santa Cruz, Institute for Particle Physics, Santa Cruz, California 95064, USA

¹⁵California Institute of Technology, Pasadena, California 91125, USA

¹⁶University of Cincinnati, Cincinnati, Ohio 45221, USA

¹⁷University of Colorado, Boulder, Colorado 80309, USA

¹⁸Colorado State University, Fort Collins, Colorado 80523, USA

¹⁹Technische Universität Dortmund, Fakultät Physik, D-44221 Dortmund, Germany

²⁰Technische Universität Dresden, Institut für Kern- und Teilchenphysik, D-01062 Dresden, Germany

²¹Laboratoire Leprince-Ringuet, CNRS/IN2P3, Ecole Polytechnique, F-91128 Palaiseau, France

²²University of Edinburgh, Edinburgh EH9 3JZ, United Kingdom

²³INFN Sezione di Ferrara^a; Dipartimento di Fisica, Università di Ferrara^b, I-44100 Ferrara, Italy

²⁴INFN Laboratori Nazionali di Frascati, I-00044 Frascati, Italy

²⁵INFN Sezione di Genova^a; Dipartimento di Fisica, Università di Genova^b, I-16146 Genova, Italy

²⁶Indian Institute of Technology Guwahati, Guwahati, Assam, 781 039, India

²⁷Harvard University, Cambridge, Massachusetts 02138, USA

²⁸Universität Heidelberg, Physikalisches Institut, Philosophenweg 12, D-69120 Heidelberg, Germany

²⁹Humboldt-Universität zu Berlin, Institut für Physik, Newtonstr. 15, D-12489 Berlin, Germany

³⁰Imperial College London, London, SW7 2AZ, United Kingdom

³¹University of Iowa, Iowa City, Iowa 52242, USA

³²Iowa State University, Ames, Iowa 50011-3160, USA

³³Johns Hopkins University, Baltimore, Maryland 21218, USA

³⁴Laboratoire de l'Accélérateur Linéaire, IN2P3/CNRS et Université Paris-Sud 11,

Centre Scientifique d'Orsay, B. P. 34, F-91898 Orsay Cedex, France

³⁵Lawrence Livermore National Laboratory, Livermore, California 94550, USA

³⁶University of Liverpool, Liverpool L69 7ZE, United Kingdom

³⁷Queen Mary, University of London, London, E1 4NS, United Kingdom

³⁸University of London, Royal Holloway and Bedford New College, Egham, Surrey TW20 0EX, United Kingdom

³⁹University of Louisville, Louisville, Kentucky 40292, USA

⁴⁰Johannes Gutenberg-Universität Mainz, Institut für Kernphysik, D-55099 Mainz, Germany

⁴¹University of Manchester, Manchester M13 9PL, United Kingdom

⁴²University of Maryland, College Park, Maryland 20742, USA

- ⁴³University of Massachusetts, Amherst, Massachusetts 01003, USA
- ⁴⁴Massachusetts Institute of Technology, Laboratory for Nuclear Science, Cambridge, Massachusetts 02139, USA
- ⁴⁵McGill University, Montréal, Québec, Canada H3A 2T8
- ⁴⁶INFN Sezione di Milano^a; Dipartimento di Fisica, Università di Milano^b, I-20133 Milano, Italy
- ⁴⁷University of Mississippi, University, Mississippi 38677, USA
- ⁴⁸Université de Montréal, Physique des Particules, Montréal, Québec, Canada H3C 3J7
- ⁴⁹INFN Sezione di Napoli^a; Dipartimento di Scienze Fisiche, Università di Napoli Federico II^b, I-80126 Napoli, Italy
- ⁵⁰NIKHEF, National Institute for Nuclear Physics and High Energy Physics, NL-1009 DB Amsterdam, The Netherlands
- ⁵¹University of Notre Dame, Notre Dame, Indiana 46556, USA
- ⁵²Ohio State University, Columbus, Ohio 43210, USA
- ⁵³University of Oregon, Eugene, Oregon 97403, USA
- ⁵⁴INFN Sezione di Padova^a; Dipartimento di Fisica, Università di Padova^b, I-35131 Padova, Italy
- ⁵⁵Laboratoire de Physique Nucléaire et de Hautes Energies, IN2P3/CNRS, Université Pierre et Marie Curie-Paris6, Université Denis Diderot-Paris7, F-75252 Paris, France
- ⁵⁶INFN Sezione di Perugia^a; Dipartimento di Fisica, Università di Perugia^b, I-06100 Perugia, Italy
- ⁵⁷INFN Sezione di Pisa^a; Dipartimento di Fisica, Università di Pisa^b; Scuola Normale Superiore di Pisa^c, I-56127 Pisa, Italy
- ⁵⁸Princeton University, Princeton, New Jersey 08544, USA
- ⁵⁹INFN Sezione di Roma^a; Dipartimento di Fisica, Università di Roma La Sapienza^b, I-00185 Roma, Italy
- ⁶⁰Universität Rostock, D-18051 Rostock, Germany
- ⁶¹Rutherford Appleton Laboratory, Chilton, Didcot, Oxon, OX11 0QX, United Kingdom
- ⁶²CEA, Irfu, SPP, Centre de Saclay, F-91191 Gif-sur-Yvette, France
- ⁶³SLAC National Accelerator Laboratory, Stanford, California 94309 USA
- ⁶⁴University of South Carolina, Columbia, South Carolina 29208, USA
- ⁶⁵Southern Methodist University, Dallas, Texas 75275, USA
- ⁶⁶Stanford University, Stanford, California 94305-4060, USA
- ⁶⁷State University of New York, Albany, New York 12222, USA
- ⁶⁸Tel Aviv University, School of Physics and Astronomy, Tel Aviv, 69978, Israel
- ⁶⁹University of Tennessee, Knoxville, Tennessee 37996, USA
- ⁷⁰University of Texas at Austin, Austin, Texas 78712, USA
- ⁷¹University of Texas at Dallas, Richardson, Texas 75083, USA
- ⁷²INFN Sezione di Torino^a; Dipartimento di Fisica Sperimentale, Università di Torino^b, I-10125 Torino, Italy
- ⁷³INFN Sezione di Trieste^a; Dipartimento di Fisica, Università di Trieste^b, I-34127 Trieste, Italy
- ⁷⁴IFIC, Universitat de Valencia-CSIC, E-46071 Valencia, Spain
- ⁷⁵University of Victoria, Victoria, British Columbia, Canada V8W 3P6
- ⁷⁶Department of Physics, University of Warwick, Coventry CV4 7AL, United Kingdom
- ⁷⁷University of Wisconsin, Madison, Wisconsin 53706, USA
- (Dated: November 30, 2018)

We report preliminary results from a study of the decay $B^0 \rightarrow \bar{D}^0 \pi^+ \pi^-$ using a data sample of 470.9 ± 2.8 million $B\bar{B}$ events collected with the BABAR detector at the $\Upsilon(4S)$ resonance. Using the Dalitz-plot analysis technique, we find contributions from the intermediate resonances $D_2^*(2460)^-$, $D_0^*(2400)^-$, $\rho(770)^0$ and $f_2(1270)$ as well as a $\pi^+ \pi^-$ S-wave term, a $\bar{D}^0 \pi^-$ nonresonant S-wave term and a virtual $D^*(2010)^-$ amplitude. We measure the branching fractions of the contributing decays.

INTRODUCTION

The study of the Dalitz plot [1] of $B^0 \rightarrow \bar{D}^0 \pi^+ \pi^-$ decays is motivated by several factors. The branching fractions of $B \rightarrow D^{**}$ transitions¹ are of interest to help address a conflict between theoretical predictions [2] and experimental results [3, 4] in semileptonic $B \rightarrow D^{**} l \nu$ decays. The $\bar{D}^0 \pi^+ \pi^-$ final state allows relatively clean studies of the $J^P = 0^+$ and 2^+ D^{**} states, since the 1^+ mesons cannot decay to $D\pi$. Measurements of these decays test theoretical models including quark models [5], QCD sum rules [6–8] and lattice QCD [9]. Similarly, measurement of the branching fraction of the $B^0 \rightarrow \bar{D}^0 \rho^0$ decay will help to test the dynamics of “color-suppression” in B decays (related to the fact that the color quantum numbers of the quarks produced from the virtual W boson must match that of the

¹ D^{**} mesons are P-wave excitations of states containing one charmed and one light (u, d) quark.

spectator quark in order for a ρ^0 meson to be formed) [10–13]. Moreover, using isospin symmetry to relate the decay amplitudes of $B^0 \rightarrow \bar{D}^0\rho^0$, $B^0 \rightarrow D^-\rho^+$ and $B^+ \rightarrow \bar{D}^0\rho^+$, it is possible to study effects of final state interactions in these decays [11, 14].

Another motivation is that the $B^0 \rightarrow \bar{D}^0\rho^0$ decay can be used to measure $\sin 2\beta$, where β is the CKM unitarity triangle angle [15, 16], if the \bar{D}^0 meson is reconstructed in a CP eigenstate. The measurement of this angle in the $\bar{b} \rightarrow \bar{c}ud$ quark-level transition is theoretically cleaner than the commonly used $\bar{b} \rightarrow \bar{c}c\bar{s}$ decays (such as $B^0 \rightarrow J/\psi K_S^0$) [17, 18] and comparisons of the values measured in different quark-level transitions can be used to search for the influence of physics beyond the Standard Model [19]. The time-dependent analysis of the $B^0 \rightarrow \bar{D}^0\pi^+\pi^-$ Dalitz plot not only allows a proper handling of effects due to interference between broad resonances, but also enables an improved measurement of β since terms proportional to $\cos 2\beta$ as well as $\sin 2\beta$ can be measured [20, 21]. For such an analysis, it is necessary to have a good understanding of the population of the $B^0 \rightarrow \bar{D}^0\pi^+\pi^-$ Dalitz plot. This can be best studied in the $\bar{D}^0 \rightarrow K^+\pi^-$ decay, which is the subject of this study.

The $B^0 \rightarrow \bar{D}^0\pi^+\pi^-$ decay has been previously studied by Belle [22] and the related $B^+ \rightarrow D^-\pi^+\pi^+$ decay has been studied by both *BABAR* [23] and Belle [24]. In this paper we present preliminary results from the first study of the $B^0 \rightarrow \bar{D}^0\pi^+\pi^-$ decay by *BABAR*. The data used in the analysis, collected with the *BABAR* detector [25] at the PEP-II asymmetric energy e^+e^- collider at SLAC, consist of an integrated luminosity of 429 fb^{-1} recorded at the $\Upsilon(4S)$ resonance (“on-peak”) and 45 fb^{-1} collected 40 MeV below the resonance (“off-peak”). The on-peak data sample contains the whole *BABAR* dataset of 470.9 ± 2.8 million $B\bar{B}$ events.

SELECTION

We reconstruct $B^0 \rightarrow \bar{D}^0\pi^+\pi^-$ candidates (the inclusion of charge conjugate reactions is implied throughout this paper) by combining a \bar{D}^0 candidate with two oppositely charged pion candidates. The charged pion candidates are required to satisfy particle identification requirements that have efficiency above 97% and kaon misidentification probability below 20%. We reconstruct \bar{D}^0 mesons in the decay channel $K^+\pi^-$. For the \bar{D}^0 daughters, the charged kaon candidates are required to satisfy particle identification requirements that have efficiency above 97% and pion misidentification probability below 15%, while the charged pion candidates are required to pass slightly looser criteria than those for the bachelor pions. The D candidates are required to have an invariant mass within $15\text{ MeV}/c^2$ of the nominal \bar{D}^0 mass [26]; this requirement is 85% efficient for signal Monte Carlo (MC) events.

The \bar{D}^0 candidate and the two bachelor pion candidates are required to originate from a common vertex. Signal events are distinguished from background using two almost uncorrelated kinematic variables: the difference ΔE between the CM energy of the B candidate and $\sqrt{s}/2$, and the beam-energy-substituted mass $m_{\text{ES}} = \sqrt{s/4 - \mathbf{p}_B^2}$, where \sqrt{s} is the total CM energy and \mathbf{p}_B is the momentum of the candidate B meson in the CM frame. We apply preselection criteria of $-0.075\text{ GeV} < \Delta E < 0.075\text{ GeV}$ and $5.272\text{ GeV}/c^2 < m_{\text{ES}} < 5.286\text{ GeV}/c^2$; these requirements are 86% efficient for signal MC events. We make further use of these kinematic variables to discriminate signal from background in the fit described below. We exclude candidates consistent with the abundant $B^0 \rightarrow D^*(2010)^-\pi^+$ decay by rejecting events which contain a candidate with $\bar{D}^0\pi^-$ invariant mass below $2.02\text{ GeV}/c^2$ (to maintain the symmetry of the Dalitz plot, we also remove the region with $\bar{D}^0\pi^+$ invariant mass below the same value). These events are used as a control sample to monitor differences between data and MC.

To suppress the background contribution from continuum $e^+e^- \rightarrow q\bar{q}$ ($q = u, d, s, c$) events, we construct a neural network (NN) discriminant that combines four variables commonly used to separate jet-like $q\bar{q}$ events from the more spherical $B\bar{B}$ events. These are: the 0th order momentum-weighted monomial moment,² L_0 ; the ratio of the 2nd order momentum-weighted monomial (L_2) to that of 0th order (L_0), L_2/L_0 ; the absolute value of the cosine of the angle between the B direction and the beam (z) axis, $|\cos\theta_{B\text{mom}}|$; and the absolute value of the cosine of the angle between the B thrust axis and the beam (z) axis, $|\cos\theta_{B\text{thr}}|$. All these variables are evaluated in the e^+e^- center-of-mass frame. We apply a requirement on the NN output that retains approximately 88% of the signal and rejects $\sim 52\%$ of the continuum background. Most of the remaining background originates from B decays, and is discussed below.

After applying all selection criteria, we retain 26334 events with candidate $B^0 \rightarrow \bar{D}^0\pi^+\pi^-$ decays. Around 20% of these events have multiple candidates. When an event has multiple candidates we retain the candidate with the best geometrical B -vertex probability.

² The momentum-weighted monomial moments are defined $L_j = \sum_i p_i |\cos\theta_i|^j$, where θ_j is the angle of the track or neutral cluster i with respect to the signal B thrust axis, p_i is its momentum, and the sum excludes the daughters of the B candidate.

The efficiency for signal events to pass all the selection criteria is determined as a function of position in the Dalitz plot (DP). Using a Monte Carlo (MC) simulation in which events uniformly populate the phase-space, we obtain an average efficiency of approximately 35%. The efficiency is shown as a function of phase-space in Figure 1, both in terms of the conventional DP (for which we choose axes $m_+^2 = m_{\bar{D}^0\pi^+}^2$ and $m_-^2 = m_{\bar{D}^0\pi^-}^2$), and in terms of the “square Dalitz plot” (SDP). The latter is described by the variables M and Θ ,

$$M \equiv \frac{1}{\pi} \arccos \left(2 \frac{m_{\pi^+\pi^-} - m_{\pi^+\pi^-}^{\min}}{m_{\pi^+\pi^-}^{\max} - m_{\pi^+\pi^-}^{\min}} - 1 \right) \quad \text{and} \quad \Theta \equiv \frac{1}{\pi} \theta_{\pi^+\pi^-}, \quad (1)$$

where $m_{\pi^+\pi^-}$ is the invariant mass of the two pions, $m_{\pi^+\pi^-}^{\max} = m_{B^0} - m_{\bar{D}^0}$ and $m_{\pi^+\pi^-}^{\min} = 2m_\pi$ are the kinematical limits of $m_{\pi^+\pi^-}$, and $\theta_{\pi^+\pi^-}$ is the angle between the \bar{D}^0 and the π^+ in the $\pi^+\pi^-$ rest frame. While the conventional DP representation provides a useful visual representation of the physics of the signal decay, the SDP allows closer scrutiny of the most densely populated regions of the phase-space, and hence is appropriate for studies of background distributions, for example.

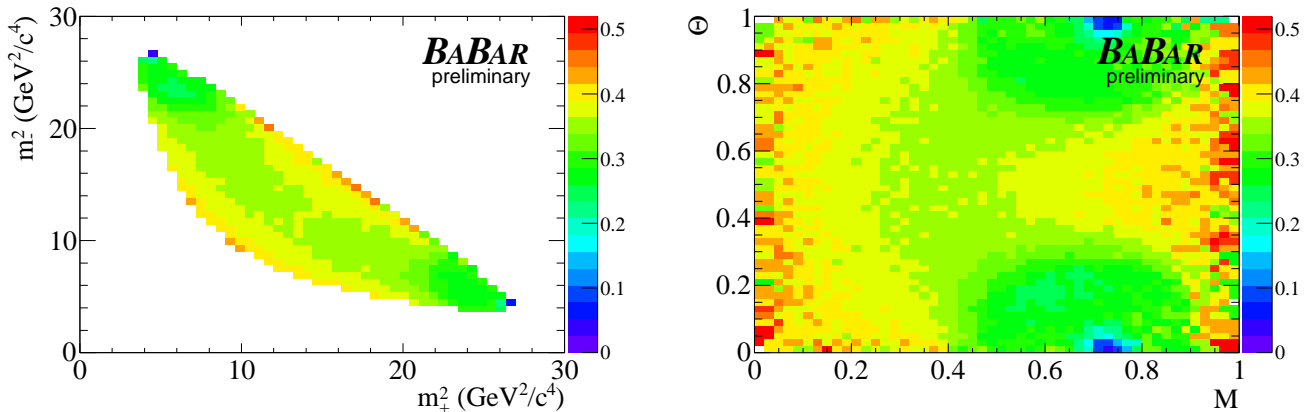


FIG. 1: Variation of the signal reconstruction efficiency over the phase-space. In these plots the $D^*(2010)^\pm$ veto is not applied.

BACKGROUNDS

In addition to the background from continuum processes, we expect backgrounds from other $B\bar{B}$ decays. These are studied using large MC samples in which the B mesons decay generically according to our current knowledge of their branching fractions. We classify backgrounds from $B\bar{B}$ decays in six categories based on their ΔE and m_{ES} distributions as determined from MC samples. The different $B\bar{B}$ background categories also have different DP distributions.

Table I lists the expected number of events and the dominant contributing mode for each category. Background categories 1 and 2 have four track final states, and peak in both ΔE and m_{ES} – category 1 has signal-like peaks in both, while category 2 has a ΔE peak shifted to positive values due to pion \rightarrow kaon misidentification. The decay modes that contribute to these categories do not contain real D mesons, with the exception of $\bar{D}^0 K_s^0$, which contributes to category 1. Background categories 3–6, which are dominant, do contain real D mesons. Category 3 peaks in m_{ES} and has a ΔE distribution that is shifted to negative values due to kaon \rightarrow pion misidentification. Categories 4–6 do not peak strongly in either ΔE or m_{ES} . Category 4 has a broad m_{ES} distribution and a slight peak in ΔE , and includes background from $D^*(2010)^-\pi^+$ events that escape the veto due to misreconstruction. Category 5 has a broad m_{ES} distribution (similar to category 4) and an approximately linear ΔE shape. Category 6 has combinatorial distributions for both m_{ES} and ΔE . The continuum background shape is combinatorial and does not peak strongly in either ΔE or m_{ES} . A summary of the backgrounds is given in Table I.

MAXIMUM LIKELIHOOD FIT

We perform an extended unbinned maximum likelihood fit using the variables ΔE , m_{ES} and the DP co-ordinates in order to determine the signal yield and the properties of the Dalitz plot. The complete likelihood function is given

TABLE I: Summary of backgrounds. For each category the dominant contributing mode and the expected number of events after all selection requirements are applied to the data are given.

Category	Dominant contribution	Total # Expected
$B\bar{B}$ 1	$J/\psi K^+\pi^-$	444 ± 24
$B\bar{B}$ 2	$a_1^\pm \pi^\mp$	32 ± 7
$B\bar{B}$ 3	$D^0 K^+\pi^-$	240 ± 18
$B\bar{B}$ 4	$\bar{D}^0 \rho^+$	7415 ± 101
$B\bar{B}$ 5	$\bar{D}^{*0} \pi^+$	1475 ± 44
$B\bar{B}$ 6	Combinatoric	7336 ± 99
$q\bar{q}$		5352 ± 226

by:

$$\mathcal{L} = \exp\left(-\sum_k N_k\right) \prod_i^{N_e} \left[\sum_k N_k \mathcal{P}_k(m_+^{2i}, m_-^{2i}, m_{\text{ES}}^i, \Delta E^i) \right], \quad (2)$$

where N_k is the event yield for species k , the index i runs over the N_e events in the data sample and \mathcal{P}_k is the probability density function (PDF) for species k , which consists of a product of the DP, m_{ES} and ΔE PDFs. The different species k are signal, $q\bar{q}$ background and six $B\bar{B}$ background categories. The function $-\ln \mathcal{L}$ is minimized to obtain the preferred values of the free parameters of the fit.

For each of the $B\bar{B}$ background categories, the ΔE , m_{ES} and DP PDFs are described with histograms obtained using MC. For $q\bar{q}$ background, the ΔE and m_{ES} PDFs are a 1st-order polynomial and an ARGUS function [27], respectively. The parameters of the ARGUS function are fixed to values determined using off-peak data, while the slope of the $q\bar{q}$ ΔE PDF is a free parameter of the fit. The continuum background DP PDF is modelled with a histogram obtained from data in a sideband region of m_{ES} , after subtraction of the (MC-based) expected contribution from $B\bar{B}$ decays in this region. We have verified the consistency of our background PDFs in off-peak data, in background MC samples, and in on-peak data sidebands. All histograms used in the fit are in the square Dalitz plot format.

The signal component is composed of two parts which are distinguished by whether or not the kinematics of the daughter particles are well reconstructed. We refer to the well reconstructed events as ‘‘correctly reconstructed’’ (CR) and the misreconstructed events as ‘‘self-cross-feed’’ (SCF). The fraction of SCF events as a function of DP position $f_{\text{SCF}}(m_+^2, m_-^2)$ is determined from MC, and is shown in Figure 2. Its value is typically below 10% but is larger in the corners of the Dalitz plot where one of the pions has low momentum.

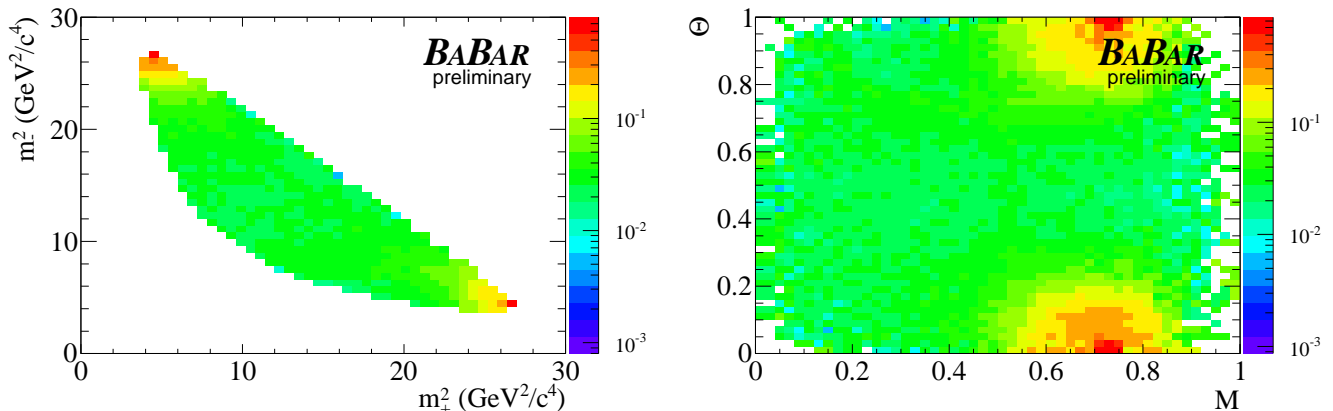


FIG. 2: Fraction of misreconstructed events as a function of the phase-space. In these plots the $D^*(2010)^\pm$ veto is not applied.

Both CR and SCF events have the same underlying physics PDF, but due to misreconstruction SCF events have reconstructed DP positions that differ from their true values. This smearing is implemented by convoluting the PDF with a resolution function $R_{\text{SCF}}(m_+^2, m_-^2; \tilde{m}_+^2, \tilde{m}_-^2)$ that gives the probability that an event with true DP position $(\tilde{m}_+^2, \tilde{m}_-^2)$ is reconstructed at (m_+^2, m_-^2) , and is described by a histogram in the square Dalitz plot co-ordinates that is itself a function of position in the phase-space. For correctly reconstructed events, DP resolution effects are negligible.

The signal Dalitz plot PDF is thus written as

$$\mathcal{P}_{\text{sig}}(m_+^2, m_-^2) = \frac{1}{\mathcal{N}} \left\{ \mathcal{P}^{\text{phys}}(m_+^2, m_-^2) \epsilon(m_+^2, m_-^2) (1 - f_{\text{SCF}}(m_+^2, m_-^2)) + \int_{\text{DP}} \left[\mathcal{P}^{\text{phys}}(\tilde{m}_+^2, \tilde{m}_-^2) \epsilon(\tilde{m}_+^2, \tilde{m}_-^2) f_{\text{SCF}}(\tilde{m}_+^2, \tilde{m}_-^2) R_{\text{SCF}}(m_+^2, m_-^2; \tilde{m}_+^2, \tilde{m}_-^2) \right] d(\tilde{m}_+^2) d(\tilde{m}_-^2) \right\}, \quad (3)$$

where $\mathcal{P}^{\text{phys}}(m_+^2, m_-^2)$ is the underlying physics PDF (discussed below), $\epsilon(m_+^2, m_-^2)$ is the efficiency (Figure 1), and $f_{\text{SCF}}(m_+^2, m_-^2)$ is the SCF fraction (Figure 2). The integral is over the Dalitz plot. The normalization factor \mathcal{N} ensures that $\mathcal{P}_{\text{sig}}(m_+^2, m_-^2)$ gives unity when integrated over the phase-space.

The CR and SCF signal events have different distributions in ΔE and m_{ES} . For m_{ES} , both CR and SCF PDFs are described by double Gaussian functions where the widths of the two Gaussians are constrained to be the same. For ΔE , the CR PDF is again a double Gaussian function (in which the two Gaussians have different widths) while the SCF PDF is represented by an asymmetric Gaussian with power-law tails. The two Gaussian widths of the ΔE PDF for the CR component are given by linear functions of $(m_{D\pi}^{\text{min}})^2 = \min(m_+^2, m_-^2)$ to account for the momentum dependence of the resolution across the DP. All SCF PDF parameters are fixed to values determined from MC, while CR PDF parameters are floated in the fit where possible. The CR PDF parameters that cannot be determined from the fit are determined from MC. Data/MC correction factors determined from the $D^*(2010)^-\pi^+$ control sample are applied to all such parameters, except for the slopes of the dependence of the ΔE widths on $(m_{D\pi}^{\text{min}})^2$.

We determine a nominal signal DP model using information from previous studies of $B^0 \rightarrow \bar{D}^0 \pi^+ \pi^-$ [22] and $B^+ \rightarrow D^- \pi^+ \pi^+$ [23, 24], and the change in the fit likelihood value observed when omitting or adding resonances. We use the isobar model [28–30], which models the total amplitude as resulting from a sum of amplitudes from the individual decay channels:

$$\mathcal{P}^{\text{phys}}(m_+^2, m_-^2) = |\mathcal{A}(m_+^2, m_-^2)|^2 \quad \text{where} \quad \mathcal{A}(m_+^2, m_-^2) = \sum_{j=1}^N c_j F_j(m_+^2, m_-^2), \quad (4)$$

where $F_j(m_+^2, m_-^2)$ are the dynamical amplitudes and c_j are complex coefficients describing the relative magnitude and phase of the different decay channels. All the weak phase dependence is contained in the c_j coefficients, which we express in terms of their real and imaginary parts: $c_j = x_j + iy_j$, so $F_j(m_+^2, m_-^2)$ contains kinematics and strong dynamics only. We treat the $\bar{D}^0 \rightarrow K^+ \pi^-$ decay as flavour-specific and neglect contributions from the doubly-Cabibbo-suppressed $D^0 \rightarrow K^+ \pi^-$ decay. We assume direct CP violation is negligible and hence use the same model for $B^0 \rightarrow \bar{D}^0 \pi^+ \pi^-$ and its conjugate decay. We also neglect possible contributions from $b \rightarrow u$ mediated, and hence highly suppressed, transitions (*e.g.* $B^0 \rightarrow D_2^*(2460)^+ \pi^-$).

In the $D\pi$ spectrum previous studies [22–24] have observed contributions from $D_2^*(2460)$ and $D_0^*(2400)$, as well as the effect of a virtual D^* ($D_v^*(2010)$) amplitude. The latter amplitude is described as virtual since although the region around the narrow $D^*(2010)$ pole is vetoed, off-shell production can contribute to the amplitude – the effect is similar to a nonresonant P-wave term. We find that an additional nonresonant (S-wave) $D\pi$ contribution is necessary to fit the data; we describe the nonresonant (NR) term using an empirical shape, first introduced in Ref. [31], proportional to $e^{-i\alpha m_-^2}$, where the shape parameter is determined from the data to be $\alpha = 0.60 \pm 0.15$ (statistical uncertainty only). In the $\pi^+ \pi^-$ spectrum previous studies [22] have observed contributions from $\rho(770)^0$ and $f_2(1270)$. We find it is necessary to include S-wave terms and hence include a contribution using the K-matrix formalism [32–34], described in more detail in the Appendix. To our knowledge, this is the first use of the K-matrix formalism in B meson decays. All other resonances are described using relativistic Breit–Wigner (RBW) shapes, with Blatt–Weisskopf barrier form factors [35] and angular distributions given in the Zemach tensor formalism [36, 37]. The Dalitz plot formalism used in this analysis is the same as that described in more detail in several previous publications [38–41]. The masses and widths of all resonances are constrained to world-average values [26], while K-matrix parameters are fixed to the values tabulated in the Appendix.

In total there are 43 free parameters of the fit. These are the yields of signal, $q\bar{q}$ and the 6 $B\bar{B}$ background categories; the real and imaginary parts of 5 intermediate contributions to the signal DP model (not counting those of $D_2^*(2460)^-\pi^+$ which are fixed as a reference); the real and imaginary parts of 10 complex coefficients in the production vector of the K-matrix parametrization of the $\pi^+ \pi^-$ S-wave; 2 parameters each of the CR signal ΔE and m_{ES} PDFs and the slope of the continuum ΔE distribution.

RESULTS

The fit returns 5098 ± 102 signal events. For this and all other quantities the statistical uncertainties are calculated from an MC study where the events are generated from the PDFs and the PDF parameters are the central values from the fit to data. Yields of the various background categories are broadly in line with expectation, although there appears to be some cross-feed between $B\bar{B}$ categories. Projections of the fit result onto m_{ES} and ΔE are shown in Figure 3, while projections onto each of the two-particle invariant masses are shown in Figure 4 and projections onto the cosines of the helicity angles, defined as the direction of one of the two daughters of the resonance relative to the direction of the third particle in the rest frame of the resonance, are shown in Figure 5. The signal distribution across the phase-space, in both conventional and square Dalitz plot co-ordinates, calculated using the *sPlot* technique [42], is shown in Figure 6. Structures due to the $D_2^*(2460)^-$, $\rho(770)^0$ and $f_2(1270)$ resonances are clearly visible.

Figures 4 and 5 show that our DP model gives an excellent representation of the data in most regions of the Dalitz plot. The only region where discrepancies between the data and the fit result are apparent is at low values of m_- , where a sharp rise near threshold is observed. This structure also appears as a reflection in the m_+ and $\cos\theta_-$ distributions. We discuss this further when we consider model uncertainties, below.

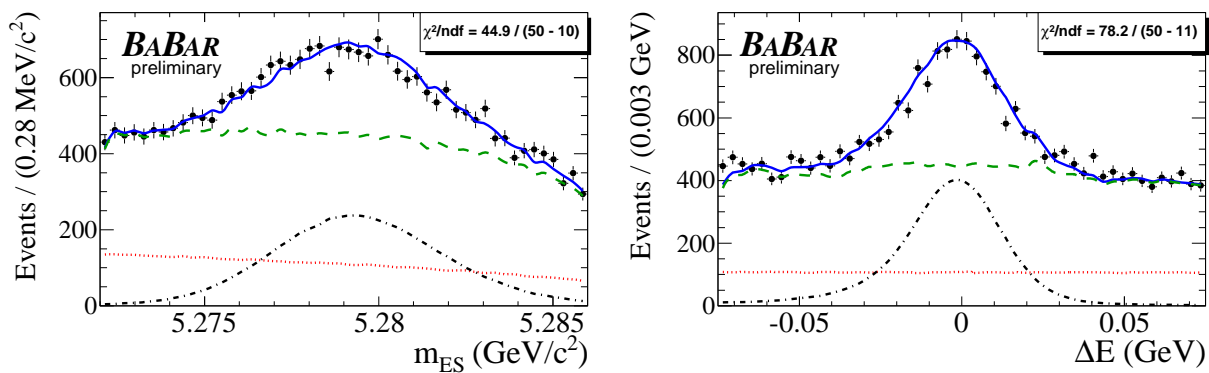


FIG. 3: m_{ES} and ΔE distributions. The points with error bars show the data, the red dotted lines show the continuum background, the green dashed lines show the total background, the black dot-dashed lines show the signal, and the blue solid lines show the total fit result.

We calculate the fit fractions and interference fit fractions, shown as a matrix in Table II. The fit fractions are the elements along the diagonal, and are given by

$$FF_j = \frac{\int_{\text{DP}} |c_j F_j(m_+^2, m_-^2)|^2 d(m_+^2) d(m_-^2)}{\int_{\text{DP}} \left| \sum_j c_j F_j(m_+^2, m_-^2) \right|^2 d(m_+^2) d(m_-^2)}, \quad (5)$$

while the interference fraction are the off-diagonal elements and are given by

$$FF_{ij} = \frac{\int_{\text{DP}} 2 \text{Re} [c_i c_j^* F_i(m_+^2, m_-^2) F_j^*(m_+^2, m_-^2)] d(m_+^2) d(m_-^2)}{\int_{\text{DP}} \left| \sum_j c_j F_j(m_+^2, m_-^2) \right|^2 d(m_+^2) d(m_-^2)}, \quad (6)$$

for $i < j$ only. Note that, with this definition, $FF_{jj} = 2FF_j$. These give a convention independent representation of the population of the DP. Although the sum of fit fractions can be greater than unity – in this case it is $(148 \pm 5)\%$ (statistical uncertainty only) – the sum including interference fit fractions must be identically equal to one. The largest interference effect is between $D_0^*(2400)^-\pi^+$ and the $D\pi$ nonresonant amplitude.

In Table III we give results for the branching fractions. The inclusive $B^0 \rightarrow \bar{D}^0 \pi^+ \pi^-$ branching fraction is calculated by dividing the signal yield by the average efficiency determined from the nominal model, by the number of $B\bar{B}$ pairs in the data sample, and by the branching fraction for the D decay ($\mathcal{B}(\bar{D}^0 \rightarrow K^+ \pi^-) = (3.91 \pm 0.05) \times 10^{-2}$ [26]). The average efficiency is found to be 30.6% and is further corrected for the measured data/MC differences (discussed under systematic uncertainties below). Our result compares well to that of Belle: $\mathcal{B}(B^0 \rightarrow \bar{D}^0 \pi^+ \pi^-) = (8.4 \pm 0.4 \pm 0.8) \times 10^{-4}$ [22]. The product branching fractions for the contributing decay modes are obtained by multiplying the

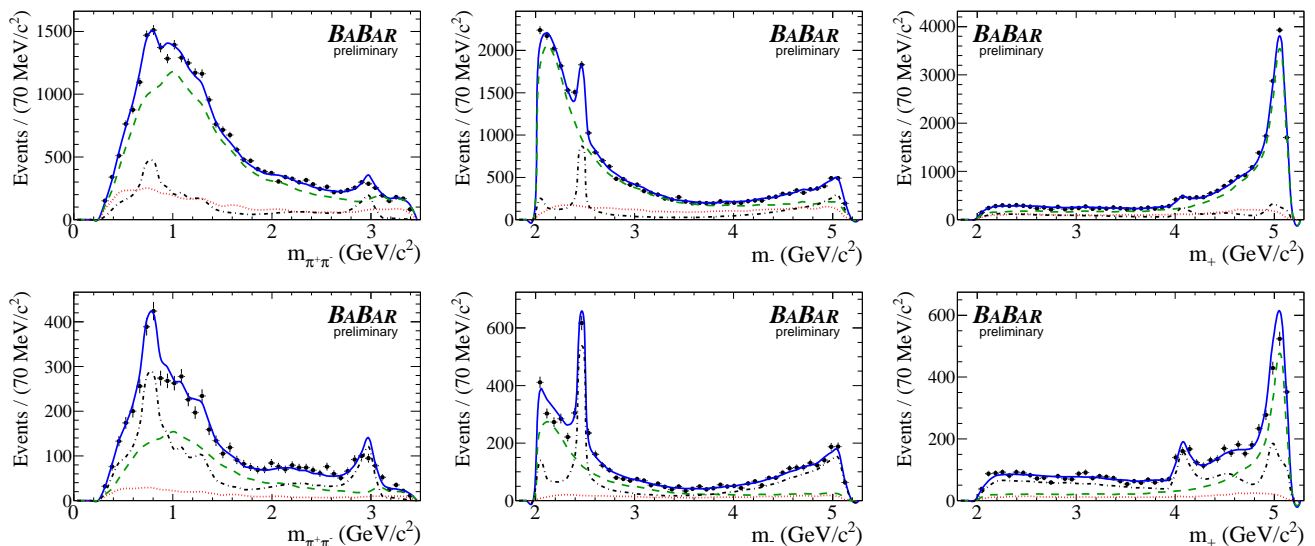


FIG. 4: Projections of the fit results onto the invariant masses. The top row shows the projection of all the data; the bottom row has the signal component enhanced by additional requirements ($5.276 \text{ GeV}/c^2 < m_{\text{ES}} < 5.282 \text{ GeV}/c^2$ and $|\Delta E| < 20 \text{ MeV}$). The points with error bars show the data, the red dotted lines show the continuum background, the green dashed lines show the total background, the black dot-dashed lines show the signal, and the blue solid lines show the total fit result.

TABLE II: Matrix of fit fractions and interference fractions (central values only without uncertainties).

	$D_2^*(2460)^-\pi^+$	$D_0^*(2400)^-\pi^+$	$\rho(770)^0\bar{D}^0$	$f_2(1270)\bar{D}^0$	$D_v^*(2010)^-\pi^+$	$D\pi$ NR	K matrix
$D_2^*(2460)^-\pi^+$	0.2047
$D_0^*(2400)^-\pi^+$	0.0000	0.2481
$\rho(770)^0\bar{D}^0$	-0.0133	0.0264	0.3343
$f_2(1270)\bar{D}^0$	-0.0130	0.0223	0.0000	0.0983
$D_v^*(2010)^-\pi^+$	0.0000	-0.0001	-0.0565	-0.0347	0.1579
$D\pi$ NR	0.0000	-0.2471	-0.0246	-0.0458	0.0001	0.1844	...
K matrix	0.0019	-0.0672	0.0000	-0.0003	-0.0016	-0.0303	0.2559

inclusive branching fraction by the relevant fit fraction. Where possible, these have also been corrected for subdecay branching fractions ($\mathcal{B}(\rho(770)^0 \rightarrow \pi^+\pi^-) = (98.9 \pm 0.16)\%$, $\mathcal{B}(f_2(1270) \rightarrow \pi^+\pi^-) = (84.8_{-1.2}^{+2.4})\%$ [26]). We are not able to perform such a calculation for $D_2^*(2460)^-\pi^+$ since, although decay modes other than $D\pi$ have been seen, the relative branching fractions are not known. The $D_0^*(2400)$ has only been observed to decay into $D\pi$, but it may be presumptuous to conclude that its branching fraction is 100%. Our results for $D_2^*(2460)^-\pi^+$, $\rho(770)^0\bar{D}^0$ and $f_2(1270)\bar{D}^0$ are consistent with those of Belle, while we see a somewhat larger branching fraction for $D_v^*(2010)^-\pi^+$ and a much larger branching fraction for $D_0^*(2400)^-\pi^+$ (Belle measures $\mathcal{B}(B^0 \rightarrow D_0^*(2400)^-\pi^+) \times \mathcal{B}(D_0^*(2400)^- \rightarrow \bar{D}^0\pi^-) = (0.60 \pm 0.13 \pm 0.15 \pm 0.22) \times 10^{-4}$).

SYSTEMATIC UNCERTAINTIES

We consider the following systematic effects on the values of the fit fractions.

- Fixed shapes of the efficiency, $q\bar{q}$ and $B\bar{B}$ Dalitz-plot histograms:
The contents of all bins of square Dalitz plot histograms used to describe these shapes are fluctuated in accordance with the uncertainties. This procedure is repeated many times and the RMS of the distribution of the change in the fit results is taken as the associated systematic uncertainty.
- Fixed m_{ES} and ΔE PDF parameters (or histograms):
We vary any fixed parameters in the PDF descriptions by their uncertainties, taking correlations into account.

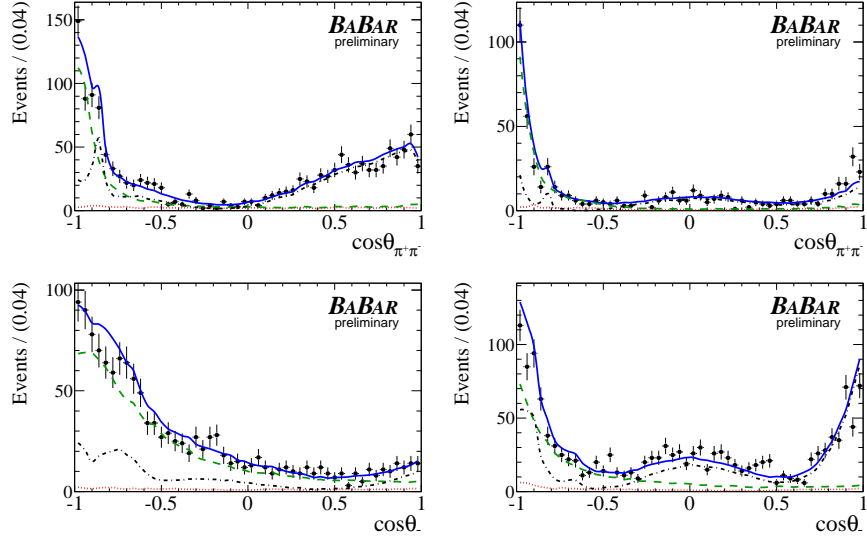


FIG. 5: Projections onto cosines of helicity angles. The signal component has been enhanced in all plots by additional cuts ($5.276 \text{ GeV}/c^2 < m_{\text{ES}} < 5.282 \text{ GeV}/c^2$ and $|\Delta E| < 20 \text{ MeV}$). The top row shows the projection onto the cosine of the $\pi^+\pi^-$ helicity angle in the regions (left) around the $\rho(770)^0$, and (right) around the $f_2(1270)$. The bottom row shows the projection onto the cosine of the $D\pi$ helicity angle in the regions (left) below and (right) around the $D_2^*(2460)$. The points with error bars show the data, the red dotted lines show the continuum background, the green dashed lines show the signal, and the blue solid lines show the total fit result.

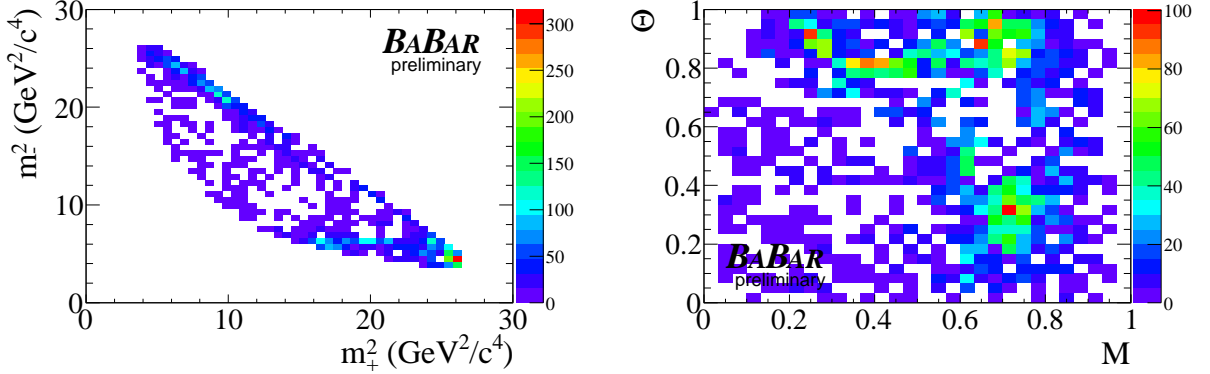


FIG. 6: sP lots of the signal distribution in the (left) Dalitz plot and (right) square Dalitz plot.

The variation in the fit results is taken as the systematic uncertainty. For most parameters, their values and uncertainties are determined from data control samples. An exception is the self-cross-feed fraction which is obtained from Monte Carlo. To conservatively allow for possible data/MC differences in the behaviour of the SCF component, we apply a Dalitz-plot independent scale factor that alternately increases and decreases the SCF fraction by a factor of two, and take the larger difference compared to the nominal result as the uncertainty. The contents of the histograms used to describe the $B\bar{B}$ background m_{ES} and ΔE PDFs are varied using the same prescription as described above.

- Fit bias:

We generate large ensembles of pseudo-experiments, containing fully simulated signal events, using the parameters returned by the fit to data. From the distribution of results of these ensembles, we evaluate biases on the fit parameters. All biases are found to be small compared to the statistical uncertainties. We assign systematic uncertainties of the sum in quadrature of half the bias and its uncertainty.

TABLE III: Branching fraction results from the fit to data. The first uncertainty is statistical, the second is systematic, the third is due to the Dalitz-plot model, and the fourth (where present) is due to secondary branching fractions. The third column gives the product of the branching fraction of the B decay to the mode listed in the leftmost column with that of the intermediate resonance decay to the final state particles.

Resonance	Fit Fraction (%)	$\mathcal{B}(B^0 \rightarrow \text{Mode}) \times \mathcal{B}(R \rightarrow hh)$ (10^{-4})	$\mathcal{B}(B^0 \rightarrow \text{Mode})$ (10^{-4})
Inclusive $B^0 \rightarrow \bar{D}^0 \pi^+ \pi^-$	$8.81 \pm 0.18 \pm 0.76 \pm 0.78 \pm 0.11$
$D_2^*(2460)^- \pi^+$	$20.5 \pm 0.9 \pm 1.3 \pm 3.7$	$1.80 \pm 0.09 \pm 0.19 \pm 0.37 \pm 0.02$...
$D_0^*(2400)^- \pi^+$	$24.8 \pm 2.5 \pm 3.0 \pm 12.9$	$2.18 \pm 0.23 \pm 0.33 \pm 1.15 \pm 0.03$...
$\rho(770)^0 \bar{D}^0$	$33.4 \pm 2.0 \pm 5.2 \pm 10.0$	$2.94 \pm 0.19 \pm 0.53 \pm 0.92 \pm 0.04$	$2.98 \pm 0.19 \pm 0.53 \pm 0.93 \pm 0.04$
$f_2(1270) \bar{D}^0$	$9.8 \pm 1.1 \pm 1.6 \pm 3.4$	$0.86 \pm 0.10 \pm 0.16 \pm 0.31 \pm 0.01$	$1.02 \pm 0.12 \pm 0.18 \pm 0.36 \pm 0.03$
$D_v^*(2010)^- \pi^+$	$15.8 \pm 0.9 \pm 1.2 \pm 3.7$	$1.39 \pm 0.08 \pm 0.16 \pm 0.35 \pm 0.02$...
$D\pi$ nonresonant	$18.4 \pm 2.3 \pm 4.3 \pm 13.6$	$1.62 \pm 0.21 \pm 0.41 \pm 1.21 \pm 0.02$...
K matrix total	$25.6 \pm 2.5 \pm 3.2 \pm 6.1$	$2.26 \pm 0.22 \pm 0.34 \pm 0.58 \pm 0.03$...

TABLE IV: Systematic uncertainties on the signal yield and fit fractions.

	Efficiency	$q\bar{q}$	$B\bar{B}$	CR m_{ES} & ΔE	SCF m_{ES} & ΔE	$B\bar{B}$ m_{ES} & ΔE	SCF	$q\bar{q}$ m_{ES}	Fit bias	Total
		DP PDF	DP PDFs	PDF parameters	PDF parameters	ΔE PDFs	fraction	PDF parameters		
Signal yield	6.3	19	24	35	0.7	22	302	2.1	46	310
$D_2^*(2460)^- \pi^+$ FF	0.0018	0.0036	0.0051	0.00072	0.00005	0.0033	0.010	0.00009	0.0037	0.013
$D_0^*(2400)^- \pi^+$ FF	0.003	0.016	0.024	0.00063	0.00013	0.0065	0.00096	0.00011	0.0023	0.030
$\rho(770)^0 \bar{D}^0$ FF	0.016	0.028	0.031	0.00069	0.00010	0.025	0.0078	0.00023	0.0014	0.052
$f_2(1270) \bar{D}^0$ FF	0.0054	0.0091	0.0077	0.00040	0.00005	0.0078	0.0029	0.00006	0.0011	0.016
$D_v^*(2010)^- \pi^+$ FF	0.00097	0.0028	0.0045	0.00034	0.00004	0.0027	0.0091	0.00007	0.0052	0.012
$D\pi$ NR FF	0.015	0.023	0.022	0.00052	0.00010	0.020	0.015	0.00008	0.0036	0.043
K matrix total FF	0.0057	0.014	0.015	0.00075	0.00017	0.012	0.018	0.00008	0.010	0.032

These sources of systematic uncertainty are summarized in Table IV. The total is obtained by combining all sources in quadrature.

We consider additional systematic effects on the values of the branching fractions. These are uncertainties on the differences between the efficiencies of selection requirements on data and MC for tracking (1.0%), particle identification (4.0%), the neural network cut (3.2%), and the number of $B\bar{B}$ pairs (0.6%). Furthermore, where we have divided by a daughter branching fraction in order to isolate the B decay branching fraction, any uncertainty in the world average value used in the division also contributes systematic uncertainty.

An additional source of uncertainty in Dalitz-plot analyses arises due to the composition of the Dalitz plot. We consider the following sources of model uncertainty:

- Fixed parameters of contributing amplitudes:

We vary the masses and widths of all resonances described by RBW shapes according to the uncertainties of the world average values [26] (with the exception of the $D_0^*(2400)$ mass, which we vary by $\pm 100 \text{ MeV}/c^2$ to account for the discrepancy in the measured masses of charged and neutral isospin partners). We vary the α parameter of the $D\pi$ nonresonant contribution within its uncertainty. We change the radius parameter of the Blatt–Weisskopf factors from its nominal value of 4 GeV^{-1} to both 3 GeV^{-1} and 5 GeV^{-1} .

- Alternative parameterisations:

We use the Gounaris–Sakurai lineshape [43] as an alternative description for the $\rho(770)$ resonance. We replace the $\pi^+ \pi^-$ S-wave K-matrix term with contributions used in the analysis of $B^0 \rightarrow \bar{D}^0 \pi^+ \pi^-$ by Belle [22], namely σ (described as in Ref. [44]), $f_0(980)$ (described by the Flatté distribution [45]) and $f_0(1370)$ (RBW). To address the possible discrepancy between the data and the fit result at low values of m_- , we replace the $D\pi$ nonresonant contribution with a functional form proposed for a putative “dabba” state [46]. We have also performed a fit in which the background from $D^{*-}(2010)\pi^+$ events escaping the veto is treated as a separate (seventh) $B\bar{B}$ background category, and include the deviation in the results as a source of model uncertainty.

- Additional possible contributions:

We repeat the fit adding states to the model: $\omega(782)$, $\rho(1450)$, $D(2600)$ (both as scalar and vector) and $D(2760)$ (vector) [47].

A summary is given in Table V. The total model uncertainty is obtained by combining all sources in quadrature.

TABLE V: Dalitz-plot model uncertainties on the signal yield and fit fractions. Refer to the text for details of the model variations.

	Mass & width	$D\pi$ NR α	BW barrier radius	$\rho(770)^0$ GS lineshape	$D\pi$ S-wave “dabba”	$\pi^+\pi^-$ S-wave	
Signal yield	44	6.4	11	1.1	14	67	
$D_2^*(2460)^-\pi^+$ FF	0.028	0.0027	0.020	0.00007	0.0019	0.0052	
$D_0^*(2400)^-\pi^+$ FF	0.061	0.031	0.0098	0.00066	0.099	0.043	
$\rho(770)^0\bar{D}^0$ FF	0.045	0.0056	0.042	0.0010	0.00012	0.034	
$f_2(1270)\bar{D}^0$ FF	0.018	0.00061	0.0060	0.00058	0.0040	0.014	
$D_v^*(2010)^-\pi^+$ FF	0.018	0.0028	0.015	0.00076	0.025	0.0097	
$D\pi$ NR FF	0.10	0.024	0.021	0.0060	...	0.026	
K matrix total FF	0.023	0.0075	0.010	0.0034	0.038	...	
	Add $\omega(782)$	Add $\rho(1450)$	Add $D(2600)$ (scalar)	Add $D(2600)$ (vector)	Add $D(2760)$ (vector)	7 $B\bar{B}$ Cat.	Total
Signal yield	11	53	0.62	13	1.5	8.4	100
$D_2^*(2460)^-\pi^+$ FF	0.00019	0.0060	0.00026	0.011	0.00063	0.00088	0.037
$D_0^*(2400)^-\pi^+$ FF	0.0019	0.00091	0.0085	0.011	0.0090	0.00034	0.129
$\rho(770)^0\bar{D}^0$ FF	0.015	0.047	0.00075	0.050	0.0096	0.0015	0.100
$f_2(1270)\bar{D}^0$ FF	0.00048	0.010	0.00004	0.021	0.0021	0.00050	0.034
$D_v^*(2010)^-\pi^+$ FF	0.0015	0.0095	0.00012	0.0040	0.0016	0.00088	0.037
$D\pi$ NR FF	0.0053	0.045	0.0025	0.065	0.0036	0.0012	0.136
K matrix total FF	0.0070	0.034	0.0019	0.018	0.011	0.00073	0.061

DISCUSSION

Isospin symmetry can be used to relate the decay amplitudes of $B^0 \rightarrow \bar{D}^0\rho^0$, $B^0 \rightarrow D^-\rho^+$ and $B^+ \rightarrow \bar{D}^0\rho^+$ [11, 14, 48, 49]:

$$A(\bar{D}^0\rho^+) = \sqrt{3}A_{3/2}, \quad (7)$$

$$A(D^-\rho^+) = \sqrt{1/3}A_{3/2} + \sqrt{2/3}A_{1/2}, \quad (8)$$

$$\sqrt{2}A(\bar{D}^0\rho^0) = \sqrt{4/3}A_{3/2} - \sqrt{2/3}A_{1/2}, \quad (9)$$

where $A_{3/2}$ and $A_{1/2}$ are the amplitudes for isospin 3/2 and 1/2 final states respectively. These equations give the triangle relation

$$A(\bar{D}^0\rho^+) = A(D^-\rho^+) + \sqrt{2}A(\bar{D}^0\rho^0). \quad (10)$$

This relation can be used to determine $\cos\delta_{D\rho}$, where $\delta_{D\rho}$ is the phase between the $A_{3/2}$ and $A_{1/2}$ amplitudes, and $R_{D\rho} = |A_{1/2}/\sqrt{2}A_{3/2}|$. In QCD factorization, both of these are expected to be unity up to corrections due to final state interactions of $\mathcal{O}(\Lambda_{\text{QCD}}/m_Q)$, where Λ_{QCD} is the QCD scale and m_Q is either m_c or m_b [11]. We obtain constraints on these parameters using the same approach previously used in the $D^{(*)}\pi$ system [50, 51]. Using our result for $\mathcal{B}(B^0 \rightarrow \bar{D}^0\rho^0)$, together with world average values of $\mathcal{B}(B^0 \rightarrow D^-\rho^+)$, $\mathcal{B}(B^+ \rightarrow \bar{D}^0\rho^+)$ and the ratio of lifetimes $\tau(B^+)/\tau(B^0)$ [26], we find

$$\begin{aligned} \cos\delta_{D\rho} &= 0.998_{-0.062}^{+0.133}, \\ R_{D\rho} &= 0.68_{-0.16}^{+0.15}, \end{aligned}$$

where all sources of uncertainty are combined. These results suggest the presence of non-factorizable final state interaction effects that, in contrast to the $D^{(*)}\pi$ system, do not introduce a significant non-zero phase difference between the isospin amplitudes.

SUMMARY

We have performed a Dalitz-plot analysis of $B^0 \rightarrow \bar{D}^0\pi^+\pi^-$ decays using the whole *BABAR* dataset of 470.9 ± 2.8 million $B\bar{B}$ events. We measure the inclusive branching fraction

$$\mathcal{B}(B^0 \rightarrow \bar{D}^0\pi^+\pi^-) = (8.81 \pm 0.18 \pm 0.76 \pm 0.78 \pm 0.11) \times 10^{-4}$$

where the first uncertainty is statistical, the second is systematic, the third is due to the Dalitz-plot model, and the fourth is due to secondary branching fractions. We find the Dalitz plot to be composed of contributions from $D_2^*(2460)^-$, $D_0^*(2400)^-$, $\rho(770)^0$ and $f_2(1270)$ as well as a $\pi^+\pi^-$ S-wave, a $D\pi$ nonresonant S-wave term and a virtual $D_v^*(2010)^-$ contribution. We determine their branching fractions:

$$\begin{aligned}\mathcal{B}(B^0 \rightarrow D_2^*(2460)^-\pi^+) \times \mathcal{B}(D_2^*(2460)^- \rightarrow \bar{D}^0\pi^-) &= (1.80 \pm 0.09 \pm 0.19 \pm 0.37 \pm 0.02) \times 10^{-4}, \\ \mathcal{B}(B^0 \rightarrow D_0^*(2400)^-\pi^+) \times \mathcal{B}(D_0^*(2400)^- \rightarrow \bar{D}^0\pi^-) &= (2.18 \pm 0.23 \pm 0.33 \pm 1.15 \pm 0.03) \times 10^{-4}, \\ \mathcal{B}(B^0 \rightarrow \rho(770)^0\bar{D}^0) &= (2.98 \pm 0.19 \pm 0.53 \pm 0.93 \pm 0.04) \times 10^{-4}, \\ \mathcal{B}(B^0 \rightarrow f_2(1270)\bar{D}^0) &= (1.02 \pm 0.12 \pm 0.18 \pm 0.36 \pm 0.03) \times 10^{-4}.\end{aligned}$$

Our Dalitz plot model differs from that obtained in a previous study of $B^0 \rightarrow \bar{D}^0\pi^+\pi^-$ by Belle [22] in that (i) we use the K-matrix description of the $\pi^+\pi^-$ S-wave, instead of including separate contributions from the $f_0(600)$ (σ), $f_0(980)$ and $f_0(1370)$ scalar resonances; (ii) we include an additional $D\pi$ nonresonant S-wave term. Our results for the inclusive branching fraction and for the color-suppressed decays $B^0 \rightarrow \rho(770)^0\bar{D}^0$ and $B^0 \rightarrow f_2(1270)\bar{D}^0$ are consistent with those from Belle and (for $\rho(770)^0\bar{D}^0$) with theoretical predictions [12, 52]. However, we find the product branching fractions for the broad and narrow D^{**} states ($D_0^*(2400)$ and $D_2^*(2460)$, respectively) to have similar values. This result disagrees with the analysis by Belle, which found a much smaller value for the $D_0^*(2400)$ branching fraction.

We are grateful for the extraordinary contributions of our PEP-II colleagues in achieving the excellent luminosity and machine conditions that have made this work possible. The success of this project also relies critically on the expertise and dedication of the computing organizations that support *BABAR*. The collaborating institutions wish to thank SLAC for its support and the kind hospitality extended to them. This work is supported by the US Department of Energy and National Science Foundation, the Natural Sciences and Engineering Research Council (Canada), the Commissariat à l'Énergie Atomique and Institut National de Physique Nucléaire et de Physique des Particules (France), the Bundesministerium für Bildung und Forschung and Deutsche Forschungsgemeinschaft (Germany), the Istituto Nazionale di Fisica Nucleare (Italy), the Foundation for Fundamental Research on Matter (The Netherlands), the Research Council of Norway, the Ministry of Education and Science of the Russian Federation, Ministerio de Ciencia e Innovación (Spain), and the Science and Technology Facilities Council (United Kingdom). Individuals have received support from the Marie-Curie IEF program (European Union), the A. P. Sloan Foundation (USA) and the Binational Science Foundation (USA-Israel).

* Now at Temple University, Philadelphia, Pennsylvania 19122, USA

† Also with Università di Perugia, Dipartimento di Fisica, Perugia, Italy

‡ Also with Università di Roma La Sapienza, I-00185 Roma, Italy

§ Now at University of South Alabama, Mobile, Alabama 36688, USA

¶ Also with Università di Sassari, Sassari, Italy

- [1] R. H. Dalitz, *Phil. Mag.* **44**, 1068 (1953).
- [2] F. Jugeau, A. Le Yaouanc, L. Oliver, and J. C. Raynal, *Phys. Rev.* **D72**, 094010 (2005), hep-ph/0504206.
- [3] D. Liventsev et al. (Belle Collaboration), *Phys. Rev.* **D77**, 091503 (2008), arXiv:0711.3252 [hep-ex].
- [4] B. Aubert et al. (*BABAR* Collaboration), *Phys. Rev. Lett.* **101**, 261802 (2008), arXiv:0808.0528 [hep-ex].
- [5] V. Morenas, A. Le Yaouanc, L. Oliver, O. Pene, and J. C. Raynal, *Phys. Rev.* **D56**, 5668 (1997), hep-ph/9706265.
- [6] Y.-b. Dai and M.-q. Huang, *Phys. Rev.* **D59**, 034018 (1999), hep-ph/9807461.
- [7] N. Uraltsev, *Phys. Lett.* **B501**, 86 (2001), hep-ph/0011124.
- [8] A. Le Yaouanc, L. Oliver, O. Pene, J. C. Raynal, and V. Morenas, *Phys. Lett.* **B520**, 25 (2001), hep-ph/0105247.
- [9] B. Blossier, M. Wagner, and O. Pene (European Twisted Mass Collaboration), *JHEP* **06**, 022 (2009), arXiv:0903.2298 [hep-lat].
- [10] M. Bauer, B. Stech, and M. Wirbel, *Z. Phys.* **C34**, 103 (1987).
- [11] M. Neubert and A. A. Petrov, *Phys. Lett.* **B519**, 50 (2001), hep-ph/0108103.
- [12] C.-K. Chua, W.-S. Hou, and K.-C. Yang, *Phys. Rev.* **D65**, 096007 (2002), hep-ph/0112148.
- [13] S. Mantry, D. Pirjol, and I. W. Stewart, *Phys. Rev.* **D68**, 114009 (2003), hep-ph/0306254.
- [14] J. L. Rosner, *Phys. Rev.* **D60**, 074029 (1999), hep-ph/9903543.
- [15] N. Cabibbo, *Phys. Rev. Lett.* **10**, 531 (1963).
- [16] M. Kobayashi and T. Maskawa, *Prog. Theor. Phys.* **49**, 652 (1973).
- [17] R. Fleischer, *Phys. Lett.* **B562**, 234 (2003), hep-ph/0301255.
- [18] R. Fleischer, *Nucl. Phys.* **B659**, 321 (2003), hep-ph/0301256.
- [19] Y. Grossman and M. P. Worah, *Phys. Lett.* **B395**, 241 (1997), hep-ph/9612269.

- [20] J. Charles, A. Le Yaouanc, L. Oliver, O. Pene, and J. C. Raynal, Phys. Lett. **B425**, 375 (1998), hep-ph/9801363.
- [21] T. Latham and T. Gershon, J. Phys. **G36**, 025006 (2009), arXiv:0809.0872 [hep-ph].
- [22] A. Kuzmin et al. (Belle Collaboration), Phys. Rev. **D76**, 012006 (2007), hep-ex/0611054.
- [23] B. Aubert et al. (BABAR Collaboration), Phys. Rev. **D79**, 112004 (2009), arXiv:0901.1291 [hep-ex].
- [24] K. Abe et al. (Belle Collaboration), Phys. Rev. **D69**, 112002 (2004), hep-ex/0307021.
- [25] B. Aubert et al. (BABAR Collaboration), Nucl. Instrum. Methods Phys. Res., Sect. A **479**, 1 (2002).
- [26] C. Amsler et al. (Particle Data Group), Phys. Lett. **B667**, 1 (2008).
- [27] H. Albrecht et al. (ARGUS Collaboration), Z. Phys. **C48**, 543 (1990).
- [28] G. N. Fleming, Phys. Rev. **135**, B551 (1964).
- [29] D. Morgan, Phys. Rev. **166**, 1731 (1968).
- [30] D. Herndon, P. Soding, and R. J. Cashmore, Phys. Rev. **D11**, 3165 (1975).
- [31] A. Garmash et al. (Belle Collaboration), Phys. Rev. **D71**, 092003 (2005).
- [32] S. U. Chung et al., Annalen Phys. **4**, 404 (1995).
- [33] I. J. R. Aitchison, Nucl. Phys. **A189**, 417 (1972).
- [34] V. V. Anisovich and A. V. Sarantsev, Eur. Phys. J. **A16**, 229 (2003), hep-ph/0204328.
- [35] J. Blatt and V. E. Weisskopf, *Theoretical Nuclear Physics* (J. Wiley (New York), 1952).
- [36] C. Zemach, Phys. Rev. **133**, B1201 (1964).
- [37] C. Zemach, Phys. Rev. **140**, B97 (1965).
- [38] B. Aubert et al. (BABAR Collaboration), Phys. Rev. **D72**, 052002 (2005), hep-ex/0507025.
- [39] B. Aubert et al. (BABAR Collaboration), Phys. Rev. **D72**, 072003 (2005), [Erratum-ibid. **D74** 099903 (2006)], hep-ex/0507004.
- [40] B. Aubert et al. (BABAR Collaboration), Phys. Rev. **D78**, 012004 (2008), arXiv:0803.4451 [hep-ex].
- [41] B. Aubert et al. (BABAR Collaboration), Phys. Rev. **D79**, 072006 (2009), arXiv:0902.2051 [hep-ex].
- [42] M. Pivk and F. R. Le Diberder, Nucl. Instrum. Meth. **A555**, 356 (2005), physics/0402083.
- [43] G. J. Gounaris and J. J. Sakurai, Phys. Rev. Lett. **21**, 244 (1968).
- [44] D. V. Bugg, Phys. Lett. **B572**, 1 (2003).
- [45] S. M. Flatte, Phys. Lett. **B63**, 224 (1976).
- [46] D. V. Bugg, J. Phys. **G36**, 075003 (2009), arXiv:0901.2217 [hep-ph].
- [47] B. Aubert et al. (BABAR Collaboration), in preparation.
- [48] C.-W. Chiang and J. L. Rosner, Phys. Rev. **D67**, 074013 (2003), hep-ph/0212274.
- [49] S. Mantry, Phys. Rev. **D70**, 114006 (2004), hep-ph/0405290.
- [50] B. Aubert et al. (BABAR Collaboration), Phys. Rev. **D69**, 032004 (2004), hep-ex/0310028.
- [51] X. Prudent (2008), IAPP-T-2008-01.
- [52] Y.-Y. Keum, T. Kurimoto, H. N. Li, C.-D. Lu, and A. I. Sanda, Phys. Rev. **D69**, 094018 (2004), hep-ph/0305335.
- [53] D. Aston et al. (LASS Collaboration), Nucl. Phys. **B296**, 493 (1988).
- [54] D. Asner, Phys. Lett. **B667**, 774 (2008).
- [55] B. Aubert et al. (BABAR Collaboration), Phys. Rev. **D78**, 034023 (2008), arXiv:0804.2089 [hep-ex].

Appendix: K-matrix description of $\pi^+\pi^-$ S wave

The K-matrix formalism gives a physical description of broad overlapping states – *i.e.* it does not violate unitarity, unlike the more conventional “sum of Breit–Wigners” approach. The K-matrix formalism can be shown to reduce to more familiar forms (the Breit–Wigner lineshape for single resonances, the Flatté lineshape [45] for coupled channels, the LASS formula [53] for broad resonances interfering with nonresonant terms). Detailed descriptions of the K-matrix formalism can be found in various references [32–34, 54]. Here we give an outline of the salient features.

The scattering (“S”) matrix describes transitions from initial states $|i\rangle$ into final states $|f\rangle$ ($S_{if} = \langle f|S|i\rangle$), and can be written

$$S = I + 2i\{\rho^\dagger\}^{1/2}T\{\rho\}^{1/2}, \quad (\text{A.11})$$

where I is the identity matrix, ρ is a diagonal phase-space matrix, with elements $\rho_{ii} = 2q_i/m$ with q_i the threshold momentum, and T is the transition matrix. The unitarity requirement ($SS^\dagger = S^\dagger S = I$) gives

$$(T^{-1} + i\rho)^\dagger = T^{-1} + i\rho, \quad \Rightarrow \quad K^{-1} = T^{-1} + i\rho, \quad (\text{A.12})$$

where K is a Lorentz-invariant and Hermitian matrix which describes the decay process. This formalism was developed for scattering processes, but can also be applied to Dalitz plot analyses, with the assumption that the two “scattering” products do not interact with the third bachelor particle [33]. However, it is also necessary to include a process-dependent production vector, which accounts for the relative production rates of the different states $|i\rangle$. We refer to the “K-matrix amplitude” as a product of the production vector P and the (matrix) propagator $(I - iK\rho)^{-1}$:

$$A_i = (I - iK\rho)_{ij}^{-1} P_j \quad (\text{A.13})$$

The K matrix is expressed as

$$K_{ij}(s) = \left[f_{ij}^{\text{scatt}} \frac{1 - s_0^{\text{scatt}}}{s - s_0^{\text{scatt}}} + \sum_{\alpha} \frac{g_i^{(\alpha)} g_j^{(\alpha)}}{m_{\alpha}^2 - s} \right] \left\{ \frac{1 - s_{A0}}{s - s_{A0}} \left(s - \frac{s_A m_{\pi}^2}{2} \right) \right\}, \quad (\text{A.14})$$

where the factor $g_i^{(\alpha)}$ is the real coupling constant of the K matrix pole α (with mass m_{α}) to meson channel i , the parameters f_{ij}^{scatt} and s_0^{scatt} describe a smooth part for the K-matrix elements, and the last factor accounts for the so-called ‘‘Adler zero’’, and suppresses kinematically fake singularities near $\pi^+\pi^-$ production threshold (s represents the square of the $\pi^+\pi^-$ invariant mass). The K-matrix parameters are determined from global fits to scattering data experiments below 1900 MeV/ c^2 [34]. Note that the phase-space for $B^0 \rightarrow \bar{D}^0 \pi^+\pi^-$ extends beyond this limit, and that the K-matrix amplitude in this high- $\pi^+\pi^-$ invariant mass region is therefore an extrapolation.

The parameters unique to the production vector, by contrast, must be determined from our data. The P vector is given by

$$P_j(s) = \left[f_{1j}^{\text{prod}} \frac{1 - s_0^{\text{prod}}}{s - s_0^{\text{prod}}} + \sum_{\alpha} \frac{\beta_{\alpha} g_j^{(\alpha)}}{m_{\alpha}^2 - s} \right], \quad (\text{A.15})$$

where as before the first term in the square brackets is nonresonant-like (‘‘slowly varying’’), and the second term is resonant-like. Hence the free parameters in the Dalitz plot fit are the complex coupling and production vector parameters β_{α} and f_{1j}^{prod} (we use a fixed value of s_0^{prod}). The index j runs over the open channels for the $\pi\pi$ S -wave, which are: $\pi\pi$, KK , $\eta\eta$, $\eta\eta'$ and 4π (or multi-meson). At higher masses there are in principle more open channels, but this is not expected to affect the results significantly. Global fits to the scattering data determine the number of poles and their parameters. We use a 5 pole approximation, and give the values of all fixed parameters in the K-matrix model in Table VI. Note that all $f_{ij}^{\text{prod}} = 0$ for $i \neq 1$ since we are interested only in the $\pi\pi$ final state.

TABLE VI: K-matrix parameters from a global analysis of the available $\pi\pi$ scattering data from threshold up to 1900 MeV/ c^2 [34, 55]. Masses and coupling constants are given in GeV/ c^2 .

m_{α}	$g_{\pi^+\pi^-}^{\alpha}$	$g_{K\bar{K}}^{\alpha}$	$g_{4\pi}^{\alpha}$	$g_{\eta\eta}^{\alpha}$	$g_{\eta\eta'}^{\alpha}$
0.65100	0.22889	-0.55377	0.00000	-0.39899	-0.34639
1.20360	0.94128	0.55095	0.00000	0.39065	0.31503
1.55817	0.36856	0.23888	0.55639	0.18340	0.18681
1.21000	0.33650	0.40907	0.85679	0.19906	-0.00984
1.82206	0.18171	-0.17558	-0.79658	-0.00355	0.22358
	f_{11}^{scatt}	f_{12}^{scatt}	f_{13}^{scatt}	f_{14}^{scatt}	f_{15}^{scatt}
	0.23399	0.15044	-0.20545	0.32825	0.35412
	s_0^{scatt}	s_0^{prod}	s_{A0}	s_A	
	-3.92637	-3.0	-0.15	1	